



# ATLAS NOTE

## ATL-PHYS-PUB-2015-006

18th March 2015



### The Optimization of ATLAS Track Reconstruction in Dense Environments

The ATLAS Collaboration

#### Abstract

This note presents recent changes in the ATLAS track reconstruction chain derived from detailed studies of track reconstruction performance in dense environments. The cores of high  $p_T$  jets and  $\tau$ -leptons are environments that are characterized by charged particle separations comparable to the resolution of the Inner Detectors sensors. The ambiguity processor stage of the reconstruction chain was overhauled, including an improvement in the usage of an artificial neural network based approach to identify pixel clusters created by multiple charged particles. These changes result in a 5% improvement for the efficiency to reconstruct all three charged daughters of a hadronically decaying  $\tau$  with  $p_T$  above 600 GeV. In jets, up to 10% more pixel clusters are found on tracks in the jet core. The track reconstruction efficiency is also much less dependent on the jet  $p_T$ . A 17% efficiency gain is seen for charged particles created at a radius of 30 mm. Similarly a 10% (14%) efficiency improvement is shown in the core of high  $p_T$  light ( $b$ ) jets. For heavy-flavour jet identification, a relative 7–13% increase in  $b$ -tagging efficiency for a given light-jet rejection rate for jets with  $p_T$  greater than 100 GeV is also obtained.

# 1 Introduction

This note presents recent changes in the ATLAS track reconstruction chain derived from detailed studies of track reconstruction performance in dense environments (TIDE). The cores of high  $p_T$  jets and  $\tau$ -leptons are characterized by separations between charged particles comparable to pixel clusters dimensions. An artificial neural network (NN) based approach was introduced in 2011 to identify clusters created by multiple charged particles [1]. The usage of this information was reconsidered during a targeted overhaul of the ambiguity solving stage of the ATLAS track reconstruction chain motivated by the potential in Run II to discover new heavy particles decaying to highly boosted objects.

Section 2 contains a brief description of the detector focusing on the Inner Detector. An overview of the track reconstruction algorithm chain is given in Section 3. Section 4 states the Monte Carlo (MC) generators and samples utilized. In Section 5, changes to the pixel cluster and track reconstruction strategy are presented. Delaying the usage of the pixel cluster NN to a later stage where its ability to resolve merged clusters is enhanced due to the available track information is a major component of the change. Section 6 presents distributions of tracks-in-jet parameters summarising the changes resulting from the optimization. This note concludes with Section 7 showing the positive impact on the performance of flavour tagging algorithms for jets with  $p_T$  above 100 GeV.

## 2 The ATLAS Inner Detector

The ATLAS experiment, a multi-purpose particle detector at the LHC, is described in detail in Ref. [2].<sup>1</sup> The Inner Detector provides position measurements for charged particles in the range  $|\eta| < 2.5$  by combining information from three sub-detectors. Starting from the interaction point and focusing on the barrel region, the high-granularity silicon Pixel Detector segmented in  $R$ - $\phi$  and  $z$  covers the vertex region and typically provides four measurements per track, including the new innermost layer (layer 0), the Insertable B-Layer (IBL) [3] added for Run II. The IBL has a mean radius of 33 mm and a typical IBL pixel has a size of  $50\ \mu\text{m}$  ( $250\ \mu\text{m}$ ) in the transverse (longitudinal) direction with a thickness of 200 and  $230\ \mu\text{m}$  for the planar and 3D sensors, respectively. For the remaining three layers (1–3) of the Pixel system, located at mean radii of 50.5, 88.5, and 122.5 mm respectively, a typical pixel has a size of  $50\ \mu\text{m}$  ( $400\ \mu\text{m}$ ) in the transverse (longitudinal) direction with a thickness of  $250\ \mu\text{m}$ . The charge collected on a pixel sensor is obtained by measuring the pulse height using the time-over-threshold (ToT) technique [4]. Outside the Pixel volume, the Silicon micro-Strip Detector (SCT) has four double-sided strip layers. On one side, the strips are parallel to the beam direction and at a stereo angle of 40 mrad on the other. The information on both sides is combined on each layer to provide an average of four three-dimensional measurements. The SCT sensors are connected to binary readout chips, which do not provide information on the collected charge. The silicon detectors are complemented by the Transition Radiation Tracker (TRT), which extends track reconstruction radially for charged particles within  $|\eta| = 2.0$  while only providing  $R$ - $\phi$  information. The raw timing information is translated into calibrated drift circles that are

---

<sup>1</sup> ATLAS uses a right-handed coordinate system with its origin at the nominal interaction point (IP) in the center of the detector and the  $z$ -axis along the beam pipe. The  $x$ -axis points from the IP to the center of the LHC ring, and the  $y$ -axis points upwards. Cylindrical coordinates  $(R, \phi)$  are used in the transverse plane,  $\phi$  being the azimuthal angle around the  $z$ -axis. The pseudorapidity is defined in terms of the polar angle  $\theta$  as  $\eta = -\ln \tan(\theta/2)$ . Angular distance is measured in units of  $\Delta R \equiv \sqrt{(\Delta\eta)^2 + (\Delta\phi)^2}$ .

associated to track candidates reconstructed from the silicon detectors. The following section provides an overview of how tracks are created starting with information from each sub-detector.

### 3 The Track Reconstruction Algorithm

The following section describes the *Baseline* track reconstruction algorithm used during Run I. Charged particle reconstruction begins with the conversion of the raw data from the Pixel and SCT detectors into three-dimensional measurements referred to as *space-points*. In the Pixel Detector, each cluster equates to one space-point, while in the SCT, clusters from both sides of a strip layer must be combined to obtain a three-dimensional measurement.

As a measure of the charge collected is available from the Pixel Detector, a sophisticated approach is taken to obtain the space-point location. The charge in a pixel sensor is often collected on multiple pixels, and the total charge is predominantly determined by the incident angle of the particle with respect to the sensor. A connected component analysis (CCA) [5] groups pixels with a common edge or corner into a cluster. The charged particle's intersection point with the sensor is determined from the cluster pixel content using a linear approximation refined with a charge interpolation technique. If the spacial separation of charged particles traversing the module is only a few pixels, charge deposits overlap and the CCA algorithm reconstructs a single *merged* cluster. An artificial neural network (NN) is thereafter used to identify merged clusters [1]. Clusters are copied to create two or three so called *split* clusters if the NN output exceeded a tunable limit. Subsequently, the position and error for each split cluster is determined by additional NNs.

After cluster creation, the primary track reconstruction algorithm utilizes iterative track-finding seeded on combinations of space-points from the silicon detectors. Additional methods are employed to recover non-prompt tracks [6]. This follows current approaches to track reconstruction first introduced in the LEP experiment [7] era. A staged pattern recognition approach is used: a loose track candidate search, which allows a number of combinatorial track candidates, is followed by a stringent ambiguity processor that compares and rates the individual tracks by assigning a relative track score to each track. This section outlines the seed finding and ambiguity solving stages of the primary track reconstruction chain. Further details, including a description of TRT track extensions, can be found in Ref. [8].

#### 3.1 Iterative Combinatorial Track Finding

Seeds are formed from sets of three space-points, which maximizes the possible number of combinations while still allowing a first crude momentum estimation. The perigee parameters of a track seed, with respect to the centre of the interaction region, are estimated by assuming a perfect helical trajectory in a uniform magnetic field.

Four possible types of combinations can be made from the Pixel and SCT detector space-points.<sup>2</sup> The purity, or fraction of seeds that result in good quality tracks, varies significantly between types. Therefore seed types are considered in order of purity starting with SCT-only then pixel-only seeds. A number of criteria are placed on the seeds to maximise purity. For example, a seed-type-dependent minimum momentum and maxima of the impact parameters are imposed. Also the use of space-points in multiple

---

<sup>2</sup> A seed is composed of space-points purely from either the Pixel Detector or the SCT, or two from the Pixel Detector (SCT) and one from the SCT (Pixel Detector).

seeds is carefully controlled. Purity is further improved by requiring one additional space-point to be compatible with the seed. A combinatorial Kalman filter [9] is then used to build track candidates from the chosen seeds. The filter creates multiple track candidates per seed if more than one compatible space-point extension exists on the same layer.

The result is a very high efficiency for reconstructing primary particles<sup>3</sup> and removing tracks created from purely random collections of space-points. Obtaining this level of performance with reasonable CPU resources is partly due to the seed purity requirements mentioned above. From  $\sim 13$  space-point combinations created for an isolated charged particle traversing the entire Inner Detector, the time intensive combinatorial Kalman filter is, on average, called in its entirety 1.1 times. However, as all reasonable combinations of tracks have been made, there are a number of track candidates with incorrectly assigned space-points. This necessitates an ambiguity solving stage.

### 3.2 Track Candidates and Ambiguity Solving

In the ATLAS ambiguity processor, the track candidates considered to create the reconstructed track collection are processed individually in descending order of a track score. The track scoring follows a robust approach based largely on simple measures of the track quality. Clusters assigned to a track increase the track score according to configurable weight fractions reflecting the intrinsic resolutions and potential cluster multiplicities in the different sub-detectors. Holes<sup>4</sup> reduce the score. The  $\chi^2$  of the track fit is also considered to penalize candidates with a poor fit. Finally the logarithm of the track momentum is considered to promote energetic tracks and suppress the larger number of tracks assigned incorrect clusters at low  $p_T$ . The ambiguity solver relies on having an appropriate track score definition that puts tracks into a reasonable order.

Measurements shared by multiple track candidates are a natural consequence of having merged clusters. Unfortunately, shared measurements must be limited as they are also a strong indicator of poorly measured tracks. Identifying merged clusters correctly helps to improve the cluster assignment and track reconstruction efficiency in dense environments as well as decreases the rate at which clusters are used on multiple tracks incorrectly. This motivates the pixel NN tool introduced in Run I. To count shared clusters, a track candidate is only compared to those tracks previously accepted by the ambiguity processor. Clusters can be shared by no more than two tracks, giving preference to tracks processed first in the ambiguity solver. Also, a track can have no more than two shared clusters. A cluster is removed from a track candidate if it pushes either the candidate or an accepted track over the shared cluster limit. The track candidate is then scored again and returned to the ordered list of remaining candidates. In this way, track candidates will be rejected by the ambiguity solving process if they fail the basic quality criteria, such as hole and cluster counts.

For qualifying track candidates, a full resolution fit is performed and the track is added back into the list of candidates. If an already fitted track passes through the ambiguity processor without any interference, it will be added to the final track collection. Delaying the track fit minimizes the number of times the fitter is called which is advantageous as it is a relatively CPU intensive process.

---

<sup>3</sup> For example muon reconstruction efficiency is in excess of 99% [10].

<sup>4</sup> Holes are defined as intersections of the reconstructed track trajectory with a sensitive detector element that do not result in a cluster. These are estimated by following closely the track trajectory and comparing the clusters-on-track with the intersected modules. Inactive modules or regions such as edge areas on the silicon sensors are excluded from the hole definition.

### 3.3 Truth-Based Reconstruction

An important tool used to study tracking performance in dense environments is truth-based reconstruction in simulated events [11]. The method replaces the combinatorial seed finding by simply gathering the correct set of clusters for a given truth particle using cluster truth information. Then, if this collection satisfies the requirements on the number of holes and clusters to build a track, the ambiguity solving stage is skipped and the particle parameters are obtained from a full resolution fit. By construction, effects such as cluster formation efficiencies are included but the removal of shared clusters by the ambiguity solver is not. Therefore, the truth-based reconstruction tracks have the ideal cluster content and reconstruction efficiency given the ATLAS detector.

### 3.4 Truth-Based Track Quality

In simulation, tracks are classified using a truth score determined by the fraction of measurements originating, at least in part, from the same simulated particle. A properly reconstructed track is required to have a truth score above 70%. Such a requirement is imposed for all reconstruction efficiencies presented in this note.

*Fake* tracks are those which have a truth score below 70%. Due to the careful pruning of seeds, the majority of reconstructed fake tracks are from the mis-allocation of clusters to a track and not purely random combinations of clusters.

## 4 Samples

In order to perform detailed studies, high statistics simulated samples in focused topologies were created with several Monte Carlo generators interfaced with a full ATLAS detector simulation [12] based on the GEANT4 program [13]. These samples, with a single particle decaying into a set of close-by charged particles, are ideal for algorithm development, as is shown in Section 5. For this purpose parent particles were generated with a flat transverse momentum ( $p_T$ ) spectrum from 10 GeV to 1 TeV within  $|\eta| < 1$ . A two track sample ( $\rho \rightarrow \pi^+ \pi^-$ ) was used to study the double track efficiency. A sample consisting of a single  $\tau$ -lepton decaying to three charged hadrons ( $\tau^\pm \rightarrow \pi^+ \pi^- \pi^\pm \nu_\tau$ ) was used to test the performance when more than two particles contribute to a cluster and the parent particle has a non-zero lifetime. Finally a single  $B^+$  sample was used to study a high multiplicity of tracks from a long-lifetime parent particle, in particular charged particles created after the innermost pixel layer. The performance was then studied in a fully simulated physics process as described in Section 6. Events with a 3 TeV  $Z'$  decaying to a pair of top quarks were fully simulated by the PYTHIA 8 [14] generator using the AU2 tune [15] and the MSTW 2008 L0 [16] PDF sets. This sample includes the effect of multiple  $pp$  interactions in the same and neighbouring bunch crossings (pile-up) by overlaying minimum bias events simulated with PYTHIA 8 on each generated event. The number of overlaid events is such that the distribution of the average number of interactions per  $pp$  bunch crossing in the simulation matches that expected in the data at  $\sqrt{s} = 13$  TeV (on average 41 interactions per bunch crossing).

## 5 Ambiguity Solver Optimization

A revision of the ambiguity solver was performed to optimize track reconstruction performance in dense environments (*TIDE*). The following section describes the changes made to the Baseline reconstruction. One particular aspect of the track reconstruction chain that was improved is the treatment of the clusters formed from multiple particles. A summary of the changes is given in Section 5.3.

### 5.1 Merged cluster identification

A measure of collected charge per pixel via the ToT [4] technique and the physical location of the pixels provides the NN with enough information to identify merged clusters efficiently. However, the inherent randomness of charged particle interactions with thin silicon layers prevents the NN from ever performing perfectly. Also, the emission of  $\delta$ -rays causes difficulties as they can lead to bigger clusters and larger charge deposits compared to expectations from a single particle. The position determination can also be biased by  $\delta$ -rays. For collimated charged particles, merged clusters that are not identified can lead to exaggerated shared cluster and hole rates, which impacts the fake rate and reconstruction efficiency.

The Run I track reconstruction chain evaluated the pixel cluster NN and performed the subsequent splitting immediately after cluster reconstruction. The incident angle of the particle improves the NN performance. After cluster reconstruction, this is estimated via the physical position of the pixel module with respect to the beam-spot position. Figure 1 shows the rate of incorrectly split one-particle clusters versus the rate of non-split multi-particle clusters [1]. For the same rate at which one-particle clusters were split in Run I, a 15% increase in efficiency for correctly identifying merged clusters can be obtained if a precise incident angle measurement is used.

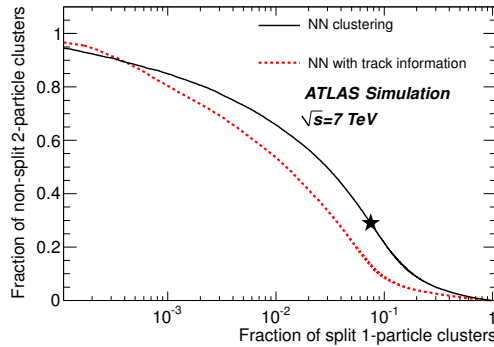


Figure 1: The fraction of split one-particle clusters versus the fraction of non-split two-particle clusters in simulation. The cut value of the NN varies along the solid and dashed lines: a tight cut corresponds to the lower right corner of the plot, and a loose cut corresponds to the upper left corner. The distribution is shown both for the NN using only the cluster and beam-spot information (solid line) and for the NN additionally including the track information (dashed line). The chosen working point for Run-I for the setup without track information is indicated with a star. The usage of this tool is discussed in Section 5.1 and full details are given in Ref. [1].

Within the ambiguity solver, the track candidate properties are precise enough to access the improved NN performance. This motivates delaying the NN evaluation until the ambiguity solver. Clusters are then no longer split or physically copied. With less clusters entering the seed finding stage, 10% fewer track candidates are produced thus saving CPU time.

After this change, the NN is consulted only when a cluster is contained in multiple track candidates. Those passing the pixel NN cut are used by the track candidates without penalty and additional NNs are used to determine the position and error of each contribution. This leads to the notion of *shareable* clusters which replaces the obsolete idea of *split* clusters. Clusters which are not shareable can still be shared but under the penalty described above.

Even with the improved performance from the precise incident angle, some merged clusters on multiple track candidates will not be identified by the NN. This can be overcome by correlating information on consecutive layers of the Pixel Detector. In general, the separation between collimated charged particles increases as they travel outward through the Inner Detector. Therefore given a merged cluster-on-track on a given layer, the next layer inward should also contain a merged cluster. Furthermore, both clusters should be used by the same track candidates. To utilise this information, if the same track candidates compete for clusters on two consecutive layers, the cluster on the inner layer will be marked shareable if the cluster on the outer layer is identified as merged by the pixel NN tool.

These changes motivate a re-optimization of the requirements on the NN outputs. With the goal of maximising efficiency against fake rate, these were loosened to 0.35 (0.4) for the two (three) particle NNs. In the next section, the optimization of four additional parameters used to control the fake rate is discussed.

The average number of truth-identified merged clusters on truth-based tracks (Section 3.3), is compared to the average number of both split and shareable clusters in Figure 2 for the single  $\rho$  and single  $\tau$  samples. The average separation of the two (three) charged particles from a  $\rho$  ( $\tau$ ) decay decreases with an increase in the parent particle momentum leading to more merged pixel clusters as shown in the points labeled *Ideal*. Both the average number of merged and shareable clusters falls to zero at the lowest parent particle  $p_T$  shown, while the Baseline reconstruction has too many split clusters due to the NN splitting single-particle clusters. The imperfect efficiency of the NN is apparent at high  $p_T$  but is a lesser problem for the TIDE optimized chain. The inefficiency is larger for the  $\tau$  sample where clusters created by more than two particles are more prevalent. The trend of the number of shareable clusters on tracks reconstructed in the TIDE optimized chain follows the true number of merged clusters nicely implying it has more physical meaning.

Cluster assignment efficiency, as shown in Figure 3 for the first two layers of the Pixel Detector, measures the fraction of clusters created by a particle that are then used on the reconstructed track of said particle. With the closest truth particle separated by  $400\ \mu\text{m}$  at the innermost layer, the cluster assignment efficiency at this layer increased from 81% (56%) to 98% (82%) per track for the  $\rho$  ( $B^+$ ) sample. A significant improvement was also achieved at all other pixel layers. Inefficiencies evident in the  $B^+$  sample are a consequence of the particle's lifetime. By decaying closer to the innermost layer, several daughter particles of the  $B^+$  are likely to contribute to a single merged cluster.

Figure 4 shows the total effect of the changes described in this note on the average number of pixel clusters on track in the  $\rho$  and three-prong  $\tau$  sample as a function of the parent particle  $p_T$ . With the improved identification of merged clusters, as shown in Figure 2, less clusters must be removed to keep track candidates below the shared cluster requirements applied during track reconstruction leading to more clusters on track. In the  $\rho$  sample, the TIDE configuration mimics the ideal content. In 3-prong  $\tau$  decays, the ideal number of clusters decreases due to the  $\tau$ 's decaying after the innermost layer. The TIDE configuration is an improvement over the Baseline, however more inefficiencies remain in events with clusters created by more than two charged particles. Changes introduced by the TIDE optimization add up to 0.3 (0.5) pixel clusters on track in the  $\rho$  ( $\tau$ ) sample.



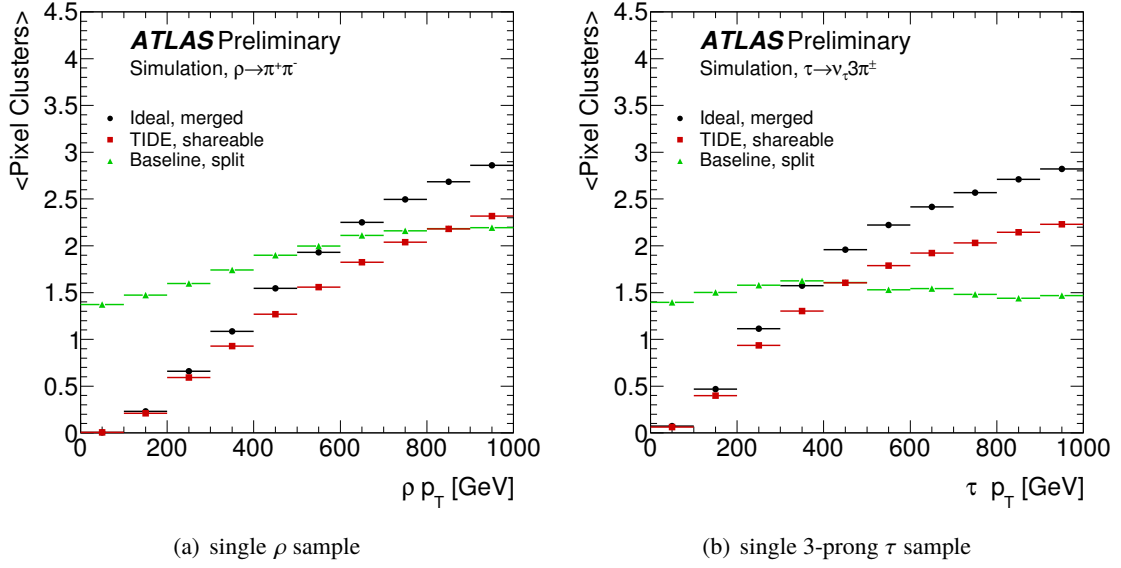


Figure 2: A comparison of the average number of merged pixel clusters on truth-based reconstruction tracks (Section 3.3) and split (shareable) pixel clusters is shown as a function of the  $\rho$  and  $\tau$  transverse momentum. The trend of the average number of shareable clusters on tracks reconstructed by the TIDE optimized chain follows the true average number of merged clusters as shown on the points labeled Ideal better than the Baseline reconstruction chain. Section 5.3 lists the full set of differences between the Baseline and TIDE reconstruction chain.

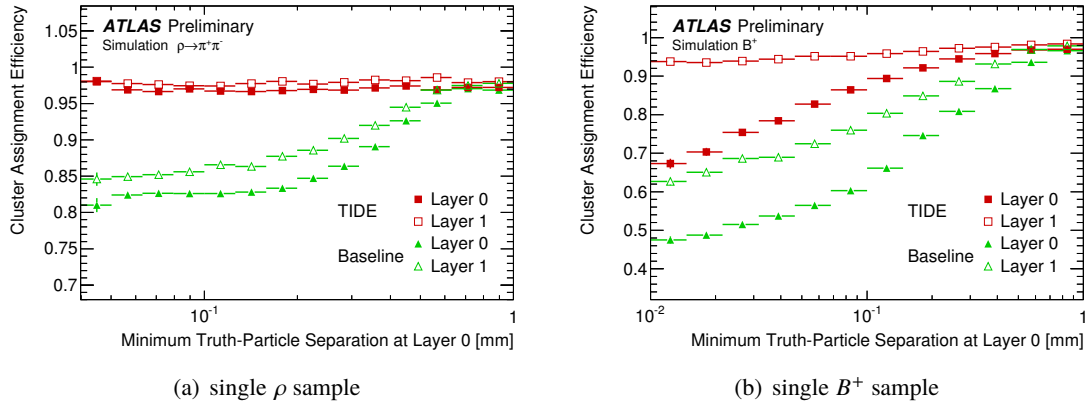


Figure 3: The efficiency by which reconstructed clusters are properly assigned to a track is shown for the two innermost pixel layers (layer 0 and layer 1) as a function of the minimum truth particle separation at layer 0. A vertical slice shows the expectation for the number of clusters on the first two layers for a given pair of tracks and their separation at layer 0. The TIDE optimized setup outperforms the baseline on both layers. Section 5.3 lists the full set of differences between the Baseline and TIDE reconstruction chain.



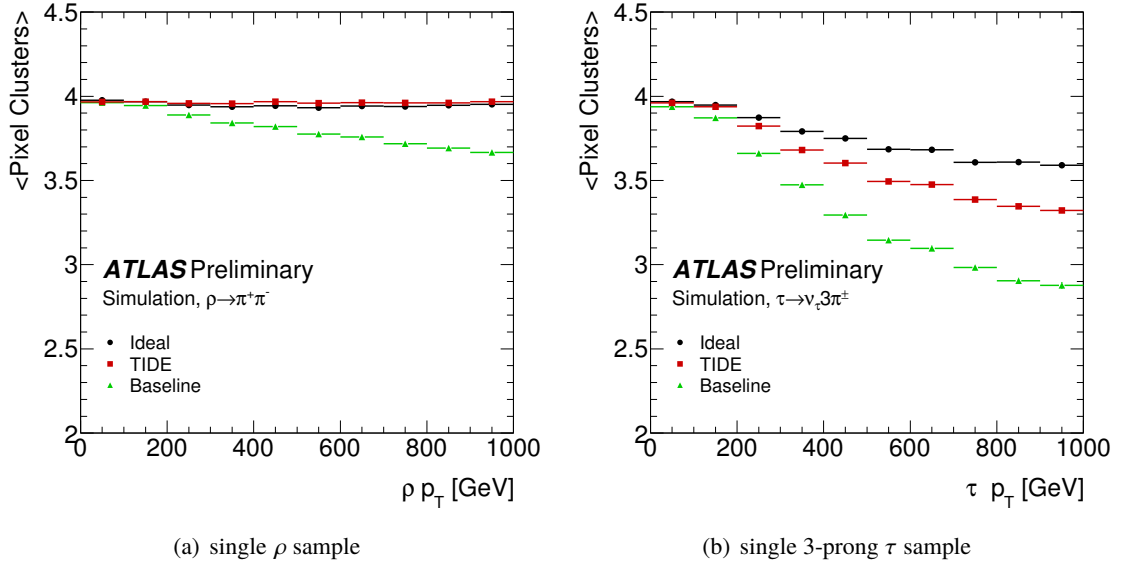


Figure 4: The average number of pixel clusters on track is shown in the  $\rho$  (a) and  $\tau$  (b) sample for the Ideal, Baseline and TIDE reconstruction as a function of the parent particle  $p_T$ . With the improved identification of merged clusters, as shown in Figure 2, less clusters are removed to keep track candidates below the requirements on shared clusters applied during track reconstruction leading to more clusters on track. In the  $\rho$  sample, the TIDE configuration mimics the ideal content. In 3-prong  $\tau$  decays, the ideal number of clusters decreases due to the  $\tau$ 's decaying after the innermost layer. The TIDE configuration is an improvement over the Baseline, however more inefficiencies remain in events with clusters created by more than two charged particles. Changes introduced by the TIDE optimization add up to 0.3 (0.5) pixel clusters on track in the  $\rho$  ( $\tau$ ) sample. Section 5.3 lists the full set of differences between the Baseline and TIDE reconstruction chain.

## 5.2 Sharing Measurements: A Trade Off

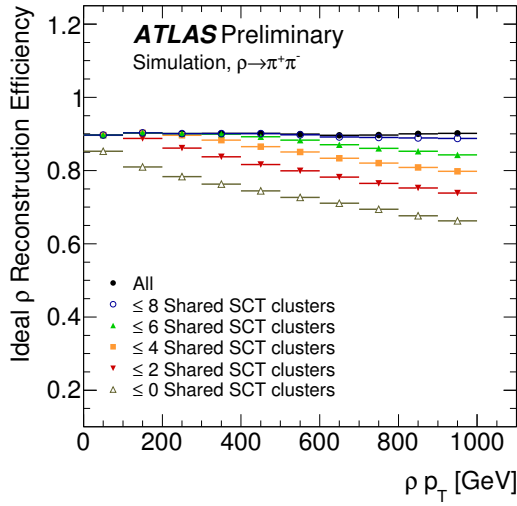
The pixel NN approach minimises the negative impact of shared pixel clusters on track reconstruction performance by helping to identify merged clusters. In the previous section, the NN was motivated as a tool used to identify merged clusters; it can also identify one-particle clusters. Clusters with a two-particle NN score less than 0.05 are explicitly forbidden from being shared. This is less a stringent requirement compared to Run I.

A multivariate strategy cannot be applied to the SCT clusters, as no information on charge deposition is available. Therefore, the requirements on shared clusters, which restrict the fake rate, can also limit the overall track reconstruction efficiency accessible in dense environments. Additional handles to control the fake rate were tuned and introduced to help with this problem. Fake rates will increase if short tracks from secondary particles are extended through incorrectly sharing clusters on the inner layers. To control this, a number of silicon clusters must be on a track before any sharing is allowed. Because of the addition of the IBL, the minimum was raised from eight to nine clusters. Two requirements were introduced to mitigate fakes. Tracks with  $p_T$  less than 1 GeV cannot have shareable clusters and a track is required to have a minimum of four unique SCT clusters.

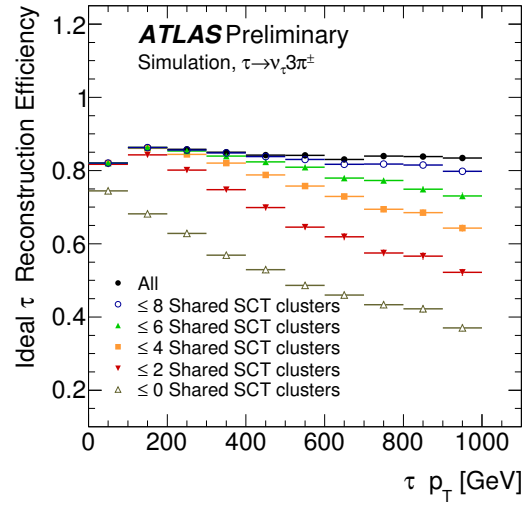
Figure 5 shows, in the  $\rho$  and  $\tau$  samples, the reconstructable, or physics, efficiency obtained from the truth-based approach described in Section 3.3. This is the maximum achievable efficiency given the cluster content requirements, including the limit on the number of shared clusters. The merged pixel clusters are assumed to have been identified and so only a cut on the number of shared SCT clusters is performed. Currently this limit is two shared clusters, as the efficiency improvement obtained from loosening this cut is not sufficient to justify the associated increase in the proportion of fake tracks.

The efficiency for reconstructing all primary tracks in events in which none are expected to have more than two shared SCT clusters is shown in Figure 6. A clear improvement in the reconstruction efficiency can be seen in the optimized setup. The improvement increases with momentum, which reflects the improved handling of multi-particle clusters in the Pixel Detector. In events without inelastic interactions, such as hadronic interactions, photon conversions, etc., the track reconstruction efficiency in the single  $\rho$  sample is very close to 100%. The efficiency is lower in the more complex  $\tau$  sample. This decrease in efficiency with momentum is caused by pattern recognition errors due to NN inefficiencies. This can reduce the truth score and cause a track to be classified as fake. The effect is amplified when looking at events where additional clusters in the detector are generated by secondary particles.

After the relaxation of the NN output requirement for clusters to be shared and other changes described in the previous section, more shared pixel clusters are expected. The effect of the changes is counterbalanced by a tightening of the way shared clusters are counted in order to keep the fake rate down at Run I levels. Previously, only the track in question was evaluated for the cluster cuts; accepted tracks were not reconsidered even if the shared cluster count changed, as more tracks were accepted. For Run II, a track will not be accepted if it fails the cluster pattern cuts *or* causes an accepted track to fail the same cuts. This increases the preference for tracks with higher score.

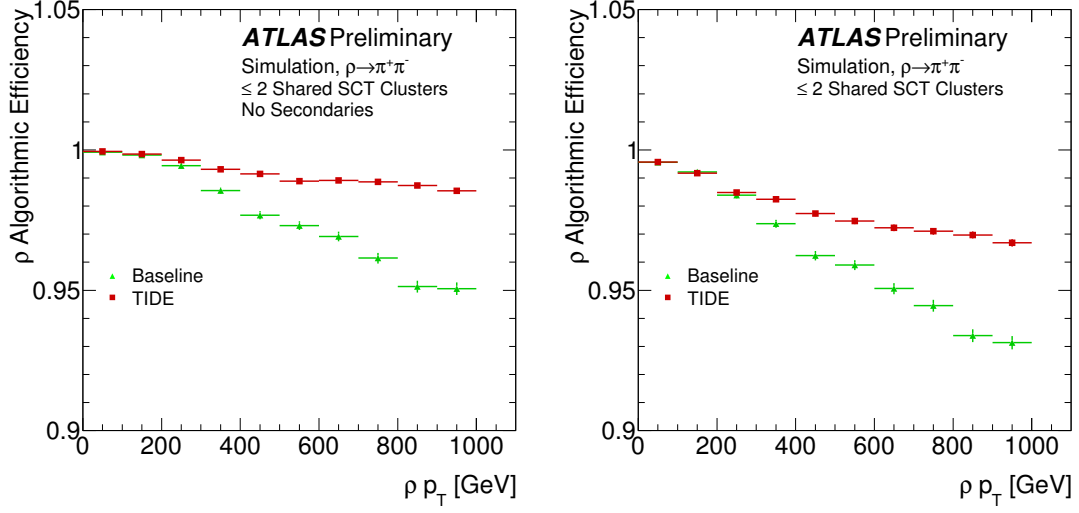


(a) single  $\rho$  sample

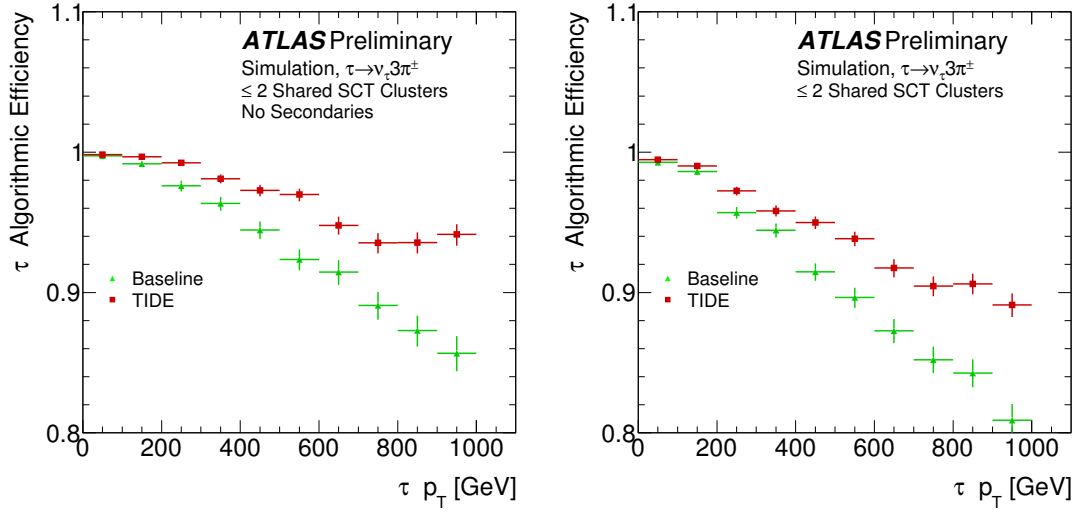


(b) single 3-prong  $\tau$  sample

Figure 5: The truth-based reconstruction (Section 3.3) efficiency is shown for reconstructing all the decay products of the  $\rho$  and the three prong  $\tau$  with various limits on the number of shared clusters allowed on a track candidate assuming all the merged pixel clusters were properly identified. The number of shared clusters is a limiting factor on the efficiency for charged particles with little spatial separation.



(a) single  $\rho$  sample



(b) single 3-prong  $\tau$  sample

Figure 6: The efficiency to reconstruct all decay products of a  $\rho$  or 3-prong  $\tau$  in events where truth-based tracks do not share more than two clusters in the SCT is shown as a function of the parent truth particle  $p_T$ . Left: events are restricted not to contain any secondary particles through nuclear interactions between the decay products and the detector material. Right: same set of plots, but no restrictions on the number of secondaries in the event. Section 5.3 lists the full set of differences between the Baseline and TIDE reconstruction chain.

### 5.3 Summary of Changes

The major driving force of the changes is delaying the decision on how to use the information encapsulated within the NN. A similar strategy of taking decisions as late in the track reconstruction chain as possible was also the theme of Ref. [7]. The following is a summary of all the changes made:

1. The evaluation of the pixel cluster NN was delayed from cluster reconstruction to the track ambiguity solver.
2. The notion of split clusters was replaced by the shareable clusters definition:
  - Pixel clusters used by multiple tracks and passing the NN selection are shareable.
  - Pixel clusters used by multiple tracks and failing the NN selection are shareable if the same tracks all use a shareable cluster on the next layer.
  - Shareable clusters can be shared without penalty (split clusters were not allowed to be shared at all).
3. Tuning of existing cuts to optimize efficiency and rejection:
  - NN output for two particle hypothesis, threshold for being shareable: 0.35
  - NN output for more than two particle hypothesis, threshold for being shareable: 0.40
  - NN output for two particle hypothesis, minimum to be allowed to be shared: 0.05
  - Minimum number of silicon clusters required to allow sharing of track's clusters: 9
4. Cuts introduced to control fake rate:
  - Minimum number of unique SCT clusters: 4
  - Minimum  $p_T$  of the track candidate to allow clusters to be shareable: 1 GeV

## 6 Track Reconstruction Performance in Jet Cores

In the previous sections, the changes to the track reconstruction chain have been described, and the impact on the performance in simple samples has been shown. These samples were crucial in understanding the problem at hand and testing alternate strategies, but they are insufficient for fine tuning and validation. The following shows the changes in cluster content of tracks within jets in fully simulated  $Z' \rightarrow t\bar{t}$  events. Truth jets are constructed from generator-level particles with the anti- $k_t$  [17] algorithm using a distance parameter of  $R = 0.4$ . Only jets with  $p_T$  greater than 100 GeV and within  $|\eta| < 2.5$  are used.

Figure 7 shows the change in the average number of clusters on the innermost pixel layer as a function of the track distance to the jet axis. A clear increase can be observed with the new (TIDE) reconstruction. The rate of having a split (for the original setup) or shareable (for the new setup) cluster on track is also shown. The number of shareable clusters increases with the particle density.

As stated above, the number of allowed shared clusters must be carefully controlled in order to balance the fake-rate and the efficiency. A consequence of the more stringent accounting of shared SCT clusters is a slight reduction in shared SCT clusters. Since the limit on shared clusters considers the entire silicon detector, a decrease in the number of shared SCT clusters allows more shared pixel clusters. Figure 8

shows how the shared cluster rate changes with the environment density for both the old and the new setup.

The resulting track reconstruction efficiency as a function of the jet's  $p_T$  is shown in Figure 9 for the old and the new setup. An increase in efficiency, especially for high jet momenta, is observed.

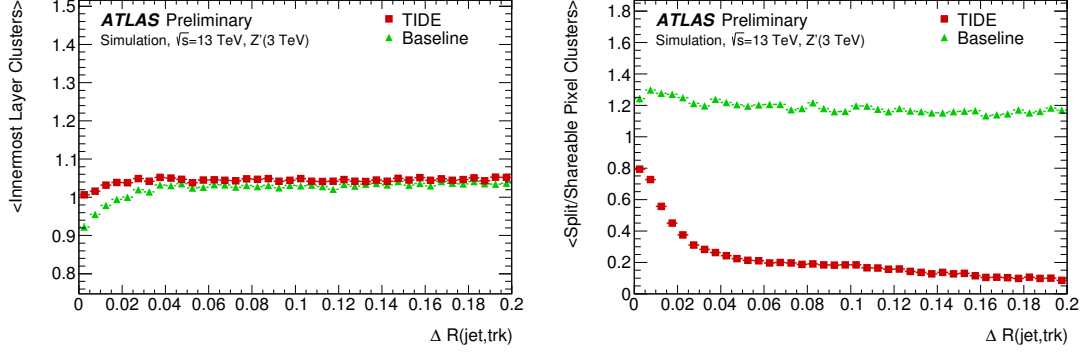


Figure 7: The average number of innermost pixel layer clusters on primary tracks (with a production vertex before the first layer) and number of split/shareable pixel clusters on these tracks are shown on the left and right respectively, as a function of the angular distance of the track from the axis of jets with  $p_T > 100$  GeV. Two track reconstruction algorithms are shown: green triangles label the baseline reconstruction (Section 3) and red squares label the TIDE optimized reconstruction (Section 5).

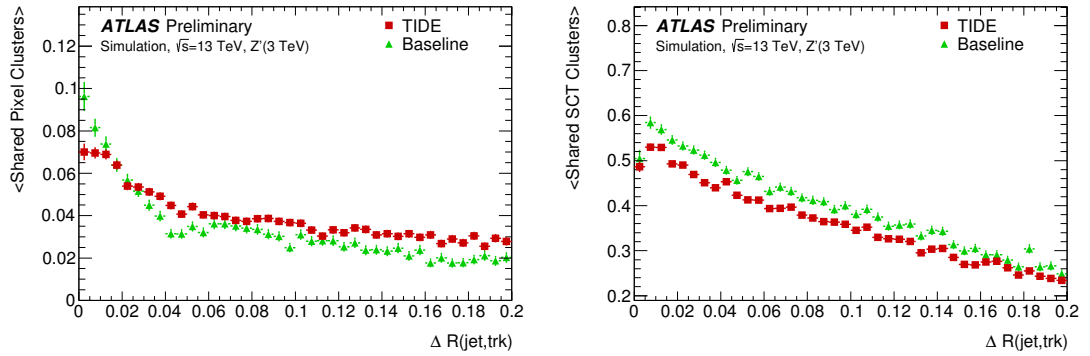


Figure 8: The average number of shared pixel (SCT) clusters for primary tracks (with a production vertex before the first layer) is shown on the left (right) as a function of the angular distance from the jet axis to the track in question. The change is expected from the changes described in Section 5.2. Two track reconstruction algorithms are shown: green triangles label the baseline reconstruction (Section 3) and red squares label the TIDE optimized reconstruction (Section 5).

Figure 10 shows the charged-primary particle reconstruction efficiency dependence on the angular distance of a particle to the jet axis and the transverse distance from the interaction vertex to where the particle was created. Jets were selected to have a  $p_T$  between 450 GeV and 750 GeV. Charged particles were required to have been created within a radius ( $R_{\text{prod}}^{\text{part}}$ ) of 100 mm and transverse the entire SCT detector ( $R_{\text{decay}}^{\text{part}} > 600$  mm). A  $p_T > 2$  GeV requirement was also used. Several particles from a displaced decay can create a single merged cluster. Clusters created from more than two particles have been shown to reduce the cluster assignment efficiency (Figure 3) and track reconstruction efficiency (Figure 6) in samples created from a single  $B^+$  and single  $\tau$ -lepton decaying to three charged hadrons respectively.

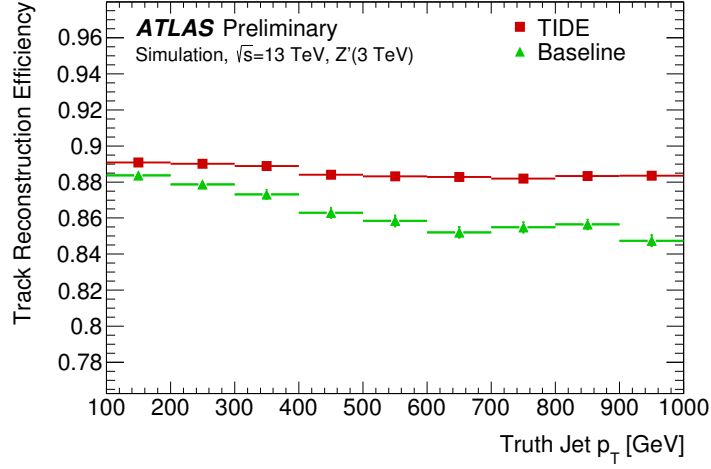


Figure 9: The average efficiency to reconstruct primary tracks with a production vertex before the first layer in jets as a function of jet  $p_T$ . The same sample generation, with limited statistics, is used for both reconstruction algorithms resulting in correlated features. Two track reconstruction algorithms are shown: green triangles label the baseline reconstruction (Section 3) and red squares label the TIDE optimized reconstruction (Section 5).

The same effect drives the reconstruction efficiency decrease towards the core of a jet in fully simulated samples. The problem is exacerbated in  $b$ -jets due to the displaced decay of heavy-flavour quarks. In all cases the new (TIDE) reconstruction provides an improvement. An approximate 17% efficiency gain is seen for charged particles created at a radius of 30 mm as well as a 10% (14%) improvement in the core of high  $p_T$  light ( $b$ ) jets.

## 7 Impact on Flavor Tagging

Jet-flavour tagging exploits the lifetime of  $b$ -quarks through the measurement of lifetime via track impact parameters or the identification and properties of displaced vertices [18]. Several taggers optimized for the different means of identification are combined in a multivariate technique. The impact parameter resolution is likely to degrade if the innermost measurement is missing or shared. In Run I, impact-parameter-based taggers considered only tracks with a cluster on the innermost layer. Therefore, this type of tagger will profit from increasing the number and precision of innermost clusters on track. Secondary vertex taggers employ multivariate discriminants using vertex properties. Such variables include the secondary vertex mass, the vertex energy fraction or the momentum of the tracks in the vertex compared to all tracks considered by the discriminant, and the secondary vertex momentum. Increasing the efficiency for highly collimated track pairs improves the secondary vertex efficiency. Also, since the collimated tracks carry a considerable fraction of the charged-particle momentum, the vertex energy fraction and vertex momentum become more discriminant.



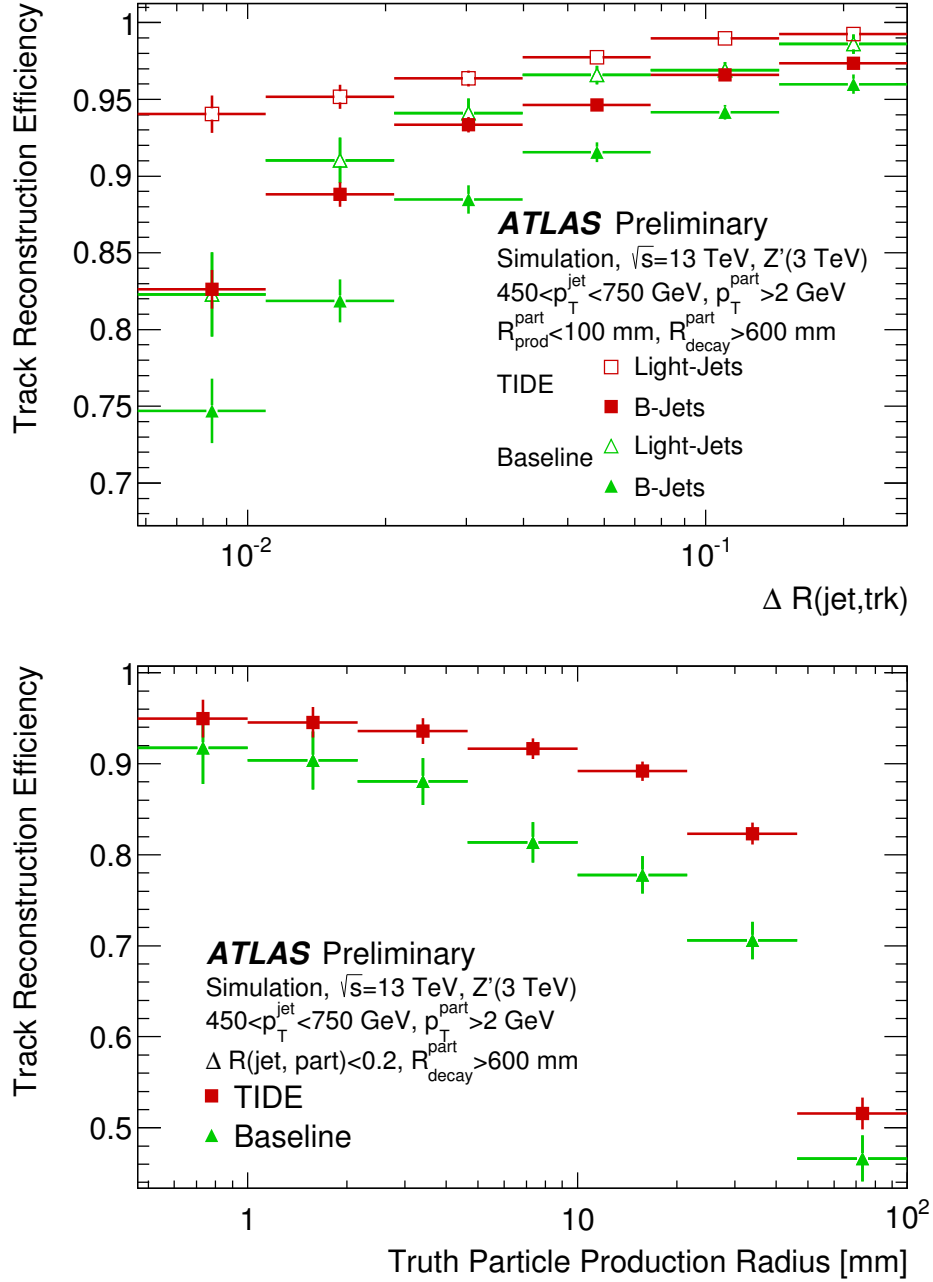


Figure 10: The average efficiency to reconstruct charged primary particles is shown as a function of the angular distance of the particle from the jet axis (top) and as a function of the production radius of the particle (bottom). Jets were selected to have a  $p_T$  between 450 GeV and 750 GeV. Charged particles were required to have been created ( $R_{\text{prod}}^{\text{part}}$ ) within 100 mm of the beam line and transverse the entire SCT detector ( $R_{\text{decay}}^{\text{part}} > 600 \text{ mm}$ ). A  $p_T > 2 \text{ GeV}$  requirement was also used. The decrease in track reconstruction efficiency in the jet core and for displaced tracks is driven by clusters created from more than two particles. Also highly displaced tracks can lack a sufficient number of clusters to be reconstructed. The new (TIDE) reconstruction provides an approximate 17% efficiency gain for charged particles created at a radius of 30 mm as well as a 10% (14%) improvement in the core of high  $p_T$  light (b) jets. Two track reconstruction algorithms are shown: green triangles label the baseline reconstruction (Section 3) and red squares label the TIDE optimized reconstruction (Section 5).

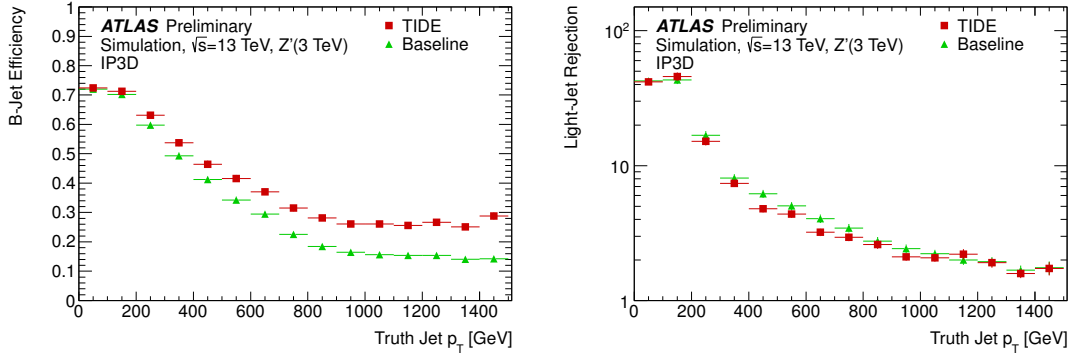


Figure 11:  $B$ -jet efficiency (left) and light-jet rejection (right) at the baseline 70% working point of the IP3D algorithm as a function of truth-jet transverse momentum. The truth jets are reconstructed from generator-level particles in  $Z'$  events, using the anti- $k_t$  algorithm with  $R=0.4$ , and are required to be within  $|\eta| < 2.5$ . The performance with the new (TIDE) reconstruction (red squares) is compared with that using the baseline reconstruction (green triangles).

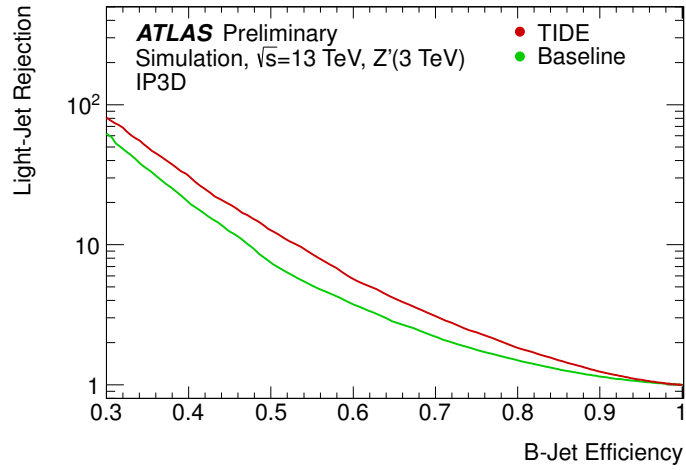


Figure 12:  $B$ -jet efficiency versus light-jet rejection for the IP3D algorithm with the new (TIDE) configuration as well as the baseline setup for anti- $k_T$   $R=0.4$  jets with  $p_T$  greater than 100 GeV and  $|\eta| < 2.5$  in a  $Z'$  sample are shown. For the baseline light-jet rejection of the commonly used 50, 60, 70, and 80%  $b$ -jet identification working points, an efficiency increase of 13, 11, 9, and 7%, respectively, is observed without retraining the likelihood.

Figure 11 shows the improvements to the impact parameter based tagger IP3D [19] for  $b$ -jet tagging efficiency as well as the effect on light-jet rejection as a function of the truth jet  $p_T$  for the  $Z'$  sample using anti- $k_t$   $R=0.4$  jets with  $|\eta| < 2.5$ . The gain in efficiency versus rejection is shown in Figure 12. A relative 13 (7)% increase in efficiency is obtained for a constant light-jet rejection rate equal to that of the 50 (80)%  $b$ -jet identification working point. A slightly reduced improvement is seen if tracks without a measurement on the innermost layer are considered in the comparison as well. The enhanced performance is driven by the increased reconstruction efficiency of displaced charged particles as shown in Figure 10. The likelihood on which the IP3D tagger is based was not retrained with tracks built using the TIDE track reconstruction. Therefore, potential for a larger increase in performance exists for this individual tagger, which is not the dominant algorithm in the final multivariate combined tagger.

## 8 Conclusion

This note presents recent changes in the ATLAS track reconstruction chain derived from detailed studies of track reconstruction in dense environments, such as the cores of high  $p_T$  jets and  $\tau$ -leptons that are characterized by charged particle separations comparable to the Inner Detector pixel cluster dimensions. The ambiguity processor stage of the reconstruction chain was optimized, including an improvement in the usage of a NN based approach to identify pixel clusters created by multiple charge particles. The changes were demonstrated with simulated samples of a single particle decaying to a set of collimated charged particles. The full impact in high  $p_T$  jets is up to 10% more IBL clusters on tracks in the jet core, a flat track-reconstruction efficiency as a function of jet  $p_T$ , and a more meaningful pixel cluster classification. A 17% efficiency gain is seen for charged particles created at a radius of 30 mm. Similarly a 10% (14%) track reconstruction efficiency improvement is shown in the core of high  $p_T$  light ( $b$ ) jets. For heavy-flavour jet identification, a relative 7–13% increase in  $b$ -tagging efficiency for a given light-jet rejection rate for jets with  $p_T$  greater than 100 GeV is also obtained. A 7-13% increase in  $b$ -jet identification of jets with  $p_T$  greater than 100 GeV is shown for a given light-jet rejection rate and a 5% improvement in the reconstruction of three-prong  $\tau$ s with  $p_T$  above 600 GeV has been demonstrated.

## References

- [1] ATLAS Collaboration, *A neural network clustering algorithm for the ATLAS silicon pixel detector*, JINST **9** (2014) P09009, arXiv: [1406.7690 \[hep-ex\]](#).
- [2] ATLAS Collaboration, *The ATLAS Experiment at the CERN Large Hadron Collider*, JINST **3** (2008) S08003.
- [3] M. Capeans et al., *ATLAS Insertable B-Layer Technical Design Report*, CERN-LHCC-2010-013. ATLAS-TDR-19 (2010), URL: <http://cdsweb.cern.ch/record/1291633>.
- [4] G. Aad et al., *ATLAS pixel detector electronics and sensors*, JINST **3** (2008) P07007, URL: <http://iopscience.iop.org/1748-0221/3/07/P07007>.
- [5] R. Rosenfeld and J. Faltz., *Sequential Operations in Digital Picture Processing*, J. ACM **13.4** (1966) 471–494, ISSN: 0004-5411, URL: <http://doi.acm.org/10.1145/321356.321357>.

- [6] T. Cornelissen et al., *Concepts, Design and Implementation of the ATLAS New Tracking (NEWT)*, ATL-SOFT-PUB-2007-007 (2007), URL: <http://cdsweb.cern.ch/record/1020106>.
- [7] D. Wicke, *A New algorithm for solving tracking ambiguities*, LC-TOOL-1999-007-TESLA (1999), URL: <http://www-library.desy.de/cgi-bin/showprep.pl?LC-TOOL-1999-007-TESLA>.
- [8] ATLAS Collaboration, *Performance of the ATLAS Silicon Pattern Recognition Algorithm in Data and Simulation at  $\sqrt{s} = 7$  TeV*, ATLAS-CONF-2010-072 (2010), URL: <http://cdsweb.cern.ch/record/1281363>.
- [9] R. Frühwirth, *Application of Kalman Filtering to Track and Vertex Fitting*, Nucl. Instrum. Meth. **A262** (1987) 444–450.
- [10] ATLAS Collaboration, *Measurement of the muon reconstruction performance of the ATLAS detector using 2011 and 2012 LHC proton–proton collision data*, Eur. Phys. J. **C74.11** (2014) 3130, arXiv: [1407.3935 \[hep-ex\]](#).
- [11] R. Jansky, *Truth Seeded Reconstruction for Fast Simulation in the ATLAS Experiment*, CERN-THESIS-2013-194 (2013), URL: <http://cdsweb.cern.ch/record/1625231/files/CERN-THESIS-2013-194.pdf>.
- [12] ATLAS Collaboration, *The ATLAS Simulation Infrastructure*, Eur.Phys.J. **C70** (2010) 823–874, arXiv: [1005.4568 \[physics.ins-det\]](#).
- [13] GEANT4 Collaboration, S. Agostinelli et al., *GEANT4—A Simulation toolkit*, Nucl.Instrum.Meth. **A506** (2003) 250–303.
- [14] T. Sjöstrand et al., *An Introduction to PYTHIA 8.2* (2014), arXiv: [1410.3012 \[hep-ph\]](#).
- [15] ATLAS Collaboration, *Summary of ATLAS Pythia 8 tunes*, ATL-PHYS-PUB-2012-003 (2012), URL: <http://cdsweb.cern.ch/record/1474107>.
- [16] A. Martin et al., *Parton distributions for the LHC*, Eur.Phys.J. **C63** (2009) 189–285, arXiv: [0901.0002 \[hep-ph\]](#).
- [17] M. Cacciari, G. P. Salam and G. Soyez, *The Anti- $k(t)$  jet clustering algorithm*, JHEP **0804** (2008) 063, arXiv: [0802.1189 \[hep-ph\]](#).
- [18] ATLAS Collaboration, *Calibration of  $b$ -tagging using dileptonic top pair events in a combinatorial likelihood approach with the ATLAS experiment*, ATLAS-CONF-2014-004 (2014), URL: <http://cdsweb.cern.ch/record/1664335>.
- [19] ATLAS Collaboration, *Commissioning of the ATLAS high-performance  $b$ -tagging algorithms in the 7 TeV collision data*, ATLAS-CONF-2011-102 (2011), URL: <http://cdsweb.cern.ch/record/1369219>.